

# Single neutral pion production by charged-current $\bar{\nu}_\mu$ interactions on hydrocarbon at $\langle E_\nu \rangle = 3.6$ GeV

T. Le<sup>a,\*</sup>, J.L. Palomino<sup>b</sup>, L. Aliaga<sup>c,k</sup>, O. Altinok<sup>d</sup>, A. Bercellie<sup>e</sup>, A. Bodek<sup>e</sup>, A. Bravar<sup>f</sup>, W.K. Brooks<sup>g</sup>, A. Butkevich<sup>h</sup>, D.A. Martinez Caicedo<sup>b,o</sup>, M.F. Carneiro<sup>b</sup>, M.E. Christy<sup>i</sup>, J. Chvojka<sup>e</sup>, H. da Motta<sup>b</sup>, J. Devan<sup>c</sup>, S.A. Dytman<sup>j</sup>, G.A. Díaz<sup>k</sup>, B. Eberly<sup>j,l</sup>, J. Felix<sup>l</sup>, L. Fields<sup>m</sup>, R. Fine<sup>e</sup>, A.M. Gago<sup>k</sup>, H. Gallagher<sup>d</sup>, R. Gran<sup>n</sup>, D.A. Harris<sup>o</sup>, A. Higuera<sup>e,l</sup>, K. Hurtado<sup>b,s</sup>, M. Kordosky<sup>c</sup>, E. Maher<sup>p</sup>, S. Manly<sup>e</sup>, W.A. Mann<sup>d</sup>, C.M. Marshall<sup>e</sup>, K.S. McFarland<sup>e,o</sup>, C.L. McGivern<sup>j</sup>, A.M. McGowan<sup>e</sup>, J. Miller<sup>g</sup>, J.G. Morfin<sup>o</sup>, J. Mousseau<sup>q</sup>, J.K. Nelson<sup>c</sup>, A. Norrick<sup>c</sup>, J. Osta<sup>o</sup>, V. Paolone<sup>j</sup>, J. Park<sup>e</sup>, C.E. Patrick<sup>m</sup>, G.N. Perdue<sup>o,e</sup>, L. Rakotondravohitra<sup>o,2</sup>, R.D. Ransome<sup>a</sup>, H. Ray<sup>q</sup>, L. Ren<sup>j</sup>, P.A. Rodrigues<sup>e</sup>, D. Ruterbories<sup>e</sup>, H. Schellman<sup>m</sup>, D.W. Schmitz<sup>r,o</sup>, J.T. Sobczyk<sup>o,3</sup>, C.J. Solano Salinas<sup>s</sup>, N. Tagg<sup>t</sup>, B.G. Tice<sup>a,4</sup>, E. Valencia<sup>l</sup>, T. Walton<sup>i</sup>, J. Wolcott<sup>e</sup>, H. Yepes-Ramirez<sup>b</sup>, G. Zavala<sup>l</sup>, D. Zhang<sup>c</sup>, B.P. Ziemer<sup>u</sup>

<sup>a</sup>Rutgers, The State University of New Jersey, Piscataway, New Jersey 08854, USA

<sup>b</sup>Centro Brasileiro de Pesquisas Físicas, Rua Dr. Xavier Sigaud 150, Urca, Rio de Janeiro, RJ, 22290-180, Brazil

<sup>c</sup>Department of Physics, College of William & Mary, Williamsburg, Virginia 23187, USA

<sup>d</sup>Physics Department, Tufts University, Medford, Massachusetts 02155, USA

<sup>e</sup>University of Rochester, Rochester, New York 14610 USA

<sup>f</sup>University of Geneva, Geneva, Switzerland

<sup>g</sup>Departamento de Física, Universidad Técnica Federico Santa María, Avenida España 1680 Casilla 110-V, Valparaíso, Chile

<sup>h</sup>Institute for Nuclear Research of the Russian Academy of Sciences, 117312 Moscow, Russia

<sup>i</sup>Hampton University, Dept. of Physics, Hampton, Virginia 23668, USA

<sup>j</sup>Department of Physics and Astronomy, University of Pittsburgh, Pittsburgh, Pennsylvania 15260, USA

<sup>k</sup>Sección Física, Departamento de Ciencias, Pontificia Universidad Católica del Perú, Apartado 1761, Lima, Perú

<sup>l</sup>Campus León y Campus Guanajuato, Universidad de Guanajuato, Lascruain de Retana No. 5, Col. Centro. Guanajuato 36000, Guanajuato México.

<sup>m</sup>Northwestern University, Evanston, Illinois 60208, USA

<sup>n</sup>Department of Physics, University of Minnesota – Duluth, Duluth, Minnesota 55812, USA

<sup>o</sup>Fermi National Accelerator Laboratory, Batavia, Illinois 60510, USA

<sup>p</sup>Massachusetts College of Liberal Arts, 375 Church Street, North Adams, Massachusetts 01247, USA

<sup>q</sup>University of Florida, Department of Physics, Gainesville, FL 32611, USA

<sup>r</sup>Enrico Fermi Institute, University of Chicago, Chicago, Illinois 60637 USA

<sup>s</sup>Universidad Nacional de Ingeniería, Apartado 31139, Lima, Perú

<sup>t</sup>Department of Physics, Otterbein University, 1 South Grove Street, Westerville, Ohio, 43081 USA

<sup>u</sup>Department of Physics and Astronomy, University of California, Irvine, Irvine, California 92697-4575, USA

## Abstract

Single neutral pion production via muon antineutrino charged-current interactions in plastic scintillator (CH) is studied using the MINERvA detector exposed to the NuMI low-energy, wideband antineutrino beam at Fermilab. Measurement of this process constrains models of neutral pion production in nuclei, which is important because the neutral-current analog is a background for  $\bar{\nu}_e$  appearance oscillation experiments. The differential cross sections for  $\pi^0$  momentum and production angle, for events with a single observed  $\pi^0$  and no charged pions, are presented and compared to model predictions. These results comprise the first measurement of the  $\pi^0$  kinematics for this process.

**Keywords:** Neutrino-nucleus scattering, Final state interaction

**PACS:** 13.15.+g, 25.80.Hp, 13.75.Gx

## 1. Introduction

Neutrino- and antineutrino-induced interactions at energies of a few GeV are a proving ground for weak interaction phenomenology in nuclei [1]. Measurements in this energy range are important because neutrino oscillation experiments [2, 3] need detailed understanding of the large variety of processes allowed. As a result, there is a growing body of new high-quality measurements for neutrino-nucleus interactions [4–7]. In particular, neutrino

\*Corresponding author

<sup>1</sup>Now at SLAC National Accelerator Laboratory, Stanford, California 94309 USA

<sup>2</sup>Also at Department of Physics, University of Antananarivo, Madagascar

<sup>3</sup>Also at Institute of Theoretical Physics, Wrocław University, Wrocław, Poland

<sup>4</sup>Now at Argonne National Laboratory, Argonne, Illinois 60439, USA

charged-current neutral pion production has become an important benchmark providing new challenges to theories describing this process [8–11].

Most of the published data for pion production in nuclei uses neutrino beams. Neutral pion production in nuclei for anti-neutrinos, however, is much less studied. Only one data point for this channel in the few-GeV energy range exists in the literature: a measurement of  $\bar{\nu}_\mu p \rightarrow \mu^+ n \pi^0$  from SKAT in a heavy liquid ( $\text{CF}_3\text{Br}$ ) bubble chamber based on 20 events at an average neutrino energy of 7 GeV [12]. Measurements of  $\pi^0$  production by neutrinos have been made in deuterium bubble chambers [13–16] and more recently on nuclear targets in the 0.1 - 1 GeV energy range using the MiniBooNE detector [17] with a mineral oil ( $\text{CH}_2$ ) target, and using the SciBar detector in K2K and SciBooNE experiments [18, 19] with plastic scintillator (CH). These recent measurements, as well as data on charged pion production [7, 20] and neutral pion production [21] have been difficult for event generators and theoretical calculations to describe accurately [8–11]. Every prediction must have a model for  $\pi^0$  production from nucleons; all use isospin decompositions within a helicity formalism that are tuned to available data [22].

Charged-current single  $\pi^0$  ( $1\pi^0$ ) production in the few-GeV region is modeled both as decays of nucleon resonances (most strongly the  $\Delta(1232)$ ) and nonresonant processes. The production in nuclei can be either direct, through the reaction  $\bar{\nu}_\mu p \rightarrow \mu^+ n \pi^0$ , or indirect, for example, through charge exchange (CEX) of a charged pion in the nucleus,  $p\pi^- \rightarrow n\pi^0$  or  $n\pi^+ \rightarrow p\pi^0$ . New data will provide useful tests of both neutrino-induced resonance production and final state interaction (FSI) models.

Neutrino interaction measurements are also important to the analysis of neutrino oscillation experiments [2, 3, 23, 24]. These experiments require the neutrino flavor be identified and the neutrino energy to be reconstructed on an event-by-event basis. An accurate modeling of these particles requires knowledge of both the underlying neutrino-nucleon interactions and of the final-state modifications that arise within the target nuclei (such as carbon) of which the massive oscillation detectors are comprised. Pion production is a source of backgrounds and systematic uncertainties in neutrino oscillation experiments. Neutral-current  $\pi^0$  production, for example, is a dominant background in  $\nu_e$  ( $\bar{\nu}_e$ ) appearance experiments because the  $\pi^0$  can mimic a final state electron (positron). In addition, experiments that reconstruct neutrino energy by identifying quasielastic events,  $\nu_\ell N(n) \rightarrow \ell^- p$  or  $\bar{\nu}_\ell N(p) \rightarrow \ell^+ n$ , interactions in which a pion is produced but then absorbed in the target nucleus can be mistaken for quasielastic signal and yield an incorrect estimate of the incident neutrino energy.

New measurements of  $1\pi^0$  production by charged-current  $\bar{\nu}_\mu$  interactions in plastic scintillator (CH) using the MINERvA detector are presented. Flux-integrated single differential cross sections as a function of  $\pi^0$  momentum and production angle for events with a single ob-

served  $\pi^0$  and no  $\pi^\pm$  exiting the interaction nucleus have been measured and are compared to predictions from the GENIE [25], NuWro [26, 27], and NEUT [28] event generators.

## 2. Experiment

The data presented here were taken using the MINERvA detector and the wideband antineutrino beam produced by the NuMI beamline in the low-energy mode [29] with a mean energy of 3.6 GeV. The antineutrino flux is estimated from a simulation of the neutrino beamline based on Geant4 [30, 31], with hadron production in the simulation constrained by proton-carbon external data [32–34]. The MINERvA detector consists of a fully active region of scintillator strips surrounded on the sides and downstream end by electromagnetic and hadronic calorimeters, and is described in detail in Ref. [35]. There are three orientations (views) for the strips (X,U,V), offset by  $60^\circ$  from each other, which enable three-dimensional reconstruction of particle trajectories. The X view is sampled twice as often as the other views. The downstream edge of the MINERvA detector is located 2 m upstream of the MINOS Near Detector, a magnetized iron spectrometer [36] used in this analysis to reconstruct the momentum and charge of muons. The transport of particles from neutrino interactions in the detector is simulated by a Geant4-based program. The readout simulation is tuned so that both the photostatistics and the reconstructed energy deposited by momentum-analyzed through-going muons agree between data and the simulation. The detector simulation of single particle responses is validated using testbeam data taken with a scaled-down version of the MINERvA detector [37].

Neutrino interactions are simulated using the GENIE 2.6.2 neutrino event generator. Details concerning GENIE and its associated parameters are described in Ref. [25]. For baryon resonance production, the formalism of Rein-Sehgal [22] is used with modern resonance properties [38]. Non-resonant pion production is simulated using the Bodek-Yang model [39] and is constrained below  $W = 1.7$  GeV by neutrino-deuterium bubble chamber data [40, 41]. Pion and nucleon FSI are modeled in GENIE using a parameterized intranuclear cascade model, with the full cascade being represented by a single interaction. For all models fitting data for light nuclei such as carbon, the pion most often has one interaction as it propagates through the nucleus. For each interaction, choice of the channel (e.g. charge exchange) is based on total cross section data and calculations [42, 43] and the kinematics and multiplicity of the final state are taken from fits to more detailed data. At the energies important for this measurement, the hadron-nucleus cross sections have large uncertainties. For example, the cross section of  $\pi^- \rightarrow \pi^0$  CEX on carbon has an uncertainty of about 50%. Reaction cross sections for  $\pi^0$  are estimated from measured cross sections for  $\pi^\pm$  scattering using isospin symmetry or theoretical models. The most significant advantages of

the single interaction used in GENIE’s FSI model are the ability to exactly reweight and to characterize each event with a single final state channel. The uncertainties in the FSI model are evaluated by varying its strength within previously measured hadron-nucleus cross-section uncertainties.

This analysis uses data taken between October 2009 and February 2012 with  $2.01 \times 10^{20}$  protons on target (POT) in the  $\bar{\nu}_\mu$  mode. About half of the exposure ( $0.945 \times 10^{20}$  POT) was taken during construction with the downstream half of the detector. In this period the ArgoNeuT detector [44] was situated between the MINERvA and MINOS Near detectors. Because the two sub-samples of the data have different efficiencies, they were analyzed separately and their results combined.

### 3. Event reconstruction and selection

The MINERvA detector records the charge and time of energy depositions (hits) in each scintillator strip. Hits are first grouped in time and then clusters of energy are formed by spatially grouping adjacent hits in each scintillator plane. Clusters with energy more than 1 MeV are then matched among the three views to create a track. The per-plane position resolution is 2.7 mm and the angular resolution of the muon track is better than 10 mrad [35] in each view. The  $\mu^+$  is identified by matching a track that exits the back of MINERvA with a positively-charged track entering the front of MINOS. The reconstruction of the muon in the MINOS spectrometer gives a typical momentum resolution of 11%. Event pile-up causes a decrease in the muon track reconstruction efficiency. This effect is studied in both MINERvA and MINOS by projecting tracks found in one of the detectors to the other and measuring the mis-reconstruction rate. This results in a  $-4.4\%$  ( $-1.1\%$ ) correction to the simulated efficiency for muons below (above) 3 GeV/c.

The event vertex, defined as the most upstream cluster on the muon track, is restricted to be within the central 108 planes of the scintillator tracking region and no closer than 22 cm to any edge of the planes. These requirements define a fiducial volume with a mass of 5.47 metric tons. Due to the requirement that the  $\mu^+$  is tracked in MINOS for charge and momentum measurement, the detection efficiency has a strong dependence on muon angle  $\theta_\mu$  and momentum  $|\vec{p}_\mu|$ , which drops to zero for events with  $\theta_\mu$  greater than 20 degrees or  $|\vec{p}_\mu|$  less than 1.0 GeV/c. The corrections for the angle and momentum efficiency are estimated from the event simulation. Only events with a single track at the vertex, the  $\mu^+$  matched to MINOS, are used in order to reject events including charged pion production. Accepted events are passed to the  $\pi^0$  reconstruction.

The neutral pion has a lifetime of  $8.52 \times 10^{-17}$  s and decays into two photons with a branching ratio of 98.8% [38], so the two photons appear to come from the event vertex. Plastic scintillator has a radiation length  $X_0 \sim 40$  cm,

which allows the two photons to convert by  $e^+e^-$  pair production or Compton scattering far away from the vertex, thus producing isolated energy deposits. The photons can also have significant energy leakage or escape the detector without conversion. Furthermore, energy deposits produced by neutrons from the same neutrino interaction can be mistaken for low-energy photon conversions, further complicating the pattern of energy deposits. The  $\pi^0$  reconstruction must correctly group these energy deposits into the two photons.

The reconstruction can be separated into two steps: pattern recognition and kinematic reconstruction. The pattern recognition builds upon the knowledge of the vertex location of the event. In the X view, clusters that are close in polar angle with respect to the vertex but can be separated in radial distance from the vertex are grouped into photon candidates. Then, for each candidate, clusters in the U and V views consistent with the stereo condition are added. Photon candidates must have clusters from at least two views for three-dimensional direction reconstruction.

In the second step, photon position, direction, and energy are determined from the clusters that have been assigned to the photons. The photon direction is reconstructed from the cluster energy-weighted slopes in each view. The photon vertex is defined by the closest cluster to the event vertex on the photon direction axis. The photon energies are reconstructed by calorimetry using calibration constants determined from the simulation. The overall calibration constant that sets the absolute energy scale is determined by matching the peak in the  $\gamma\gamma$  invariant mass distribution to the  $\pi^0$  nominal mass of 134.97 MeV/c<sup>2</sup> [38]. This procedure is done separately for data and simulation which enables correction for a difference in energy scales of 5% between the data and simulation. Finally, the  $\pi^0$  momentum is calculated from momentum conservation,  $\vec{p}_{\pi^0} = \vec{k}_1 + \vec{k}_2$ , where  $\vec{k}_i$  are reconstructed photon momenta. The  $\pi^0$  is reconstructed with a 25% energy resolution and 3.5 degrees angular resolution in each view. The incoming neutrino energy is reconstructed from the  $\mu^+$  and  $\pi^0$  4-momenta using

$$\begin{aligned} E_\nu^{rec} &= E_\mu + E_{\pi^0} + T_n \\ T_n &= \frac{1}{2} \frac{[(E_\mu - p_\mu^\parallel) + (E_{\pi^0} - p_{\pi^0}^\parallel)]^2 + (\vec{p}_\mu^\perp + \vec{p}_{\pi^0}^\perp)^2}{m_N - (E_\mu - p_\mu^\parallel) - (E_{\pi^0} - p_{\pi^0}^\parallel)}, \end{aligned} \quad (1)$$

where  $\vec{p}^\perp, p^\parallel$  are the transverse and longitudinal components of momentum, respectively. It is assumed that the initial nucleon is at rest and that the  $\pi^0$  is produced together with a nucleon. The neutrino energy is reconstructed with 10% resolution. The  $\gamma\gamma$  invariant mass  $m_{\gamma\gamma}$  is reconstructed from the photon energies  $E_{1,2}$  and the separation angle  $\theta_{\gamma\gamma}$  between the two photons using

$$m_{\gamma\gamma}^2 = 2E_1E_2(1 - \cos\theta_{\gamma\gamma}). \quad (2)$$

The two reconstructed photons are required to convert at least 15 cm ( $0.36X_0$ ) away from the vertex to further reject charged-pion backgrounds. In addition, it is required

that  $E_\nu^{rec}$  is between 1.5 and 20 GeV. The lower energy cut is needed due to MINOS acceptance while the upper cut is to reduce flux uncertainties. Finally, it is required that  $m_{\gamma\gamma}$  is between 75 MeV/ $c^2$  and 195 MeV/ $c^2$ . The selected sample has 1304 events. The total selection efficiency is 6% and purity 55%, according to the simulation. The background is dominated (70% of the total background) by events with at least one  $\pi^0$  in the detector. Half of this is due to multi-pion production,  $\pi^0 + \pi^\pm$ , where the  $\pi^\pm$  is not tracked, while the other half has a secondary  $\pi^0$  produced by  $\pi^- \rightarrow \pi^0$  CEX or nucleon scattering in the detector but outside the primary interaction nucleus. The non- $\pi^0$  background is mostly due to energy deposits by  $\pi^-$  and neutrons which are mistakenly identified as photons, and accounts for the remaining 30% of the total background.

Figure 1 shows the  $m_{\gamma\gamma}$  distributions for both data and simulation of the selected sample before the invariant mass cut. There is a clear peak centered around the  $\pi^0$  nominal mass in both data and simulation. The distribution from simulation is broken down into signal and background components. The signal is defined as antineutrino charged-current events with single  $\pi^0$  and no  $\pi^\pm$  escaping the nucleus. The background is anything else that is not signal. By this definition, it is possible for signal events to have the  $\pi^0$ s mis-reconstructed from non- $\pi^0$  energy deposits. The signal events at high  $m_{\gamma\gamma}$ , outside the signal mass width, have one or both candidate photons reconstructed from neutron energy deposits. The same mis-reconstruction happens to signal events in the selected sample but at a smaller rate (14%). The  $\pi^0$  momentum and angular shapes of these events are found to be similar to the rest of the signal events. The enhancement in the background distribution around the  $\pi^0$  mass is due to background events with at least one  $\pi^0$  in the detector.

After event selection, the selected sample still has substantial background to be subtracted statistically from the total distribution for each observable. The background distribution for each observable is estimated from the simulation with the total background rate constrained by data. This significantly reduces the uncertainties in the estimated background. The background rate is determined from a binned extended maximum likelihood fit of an invariant mass model to the data [45]. The invariant mass model  $M(m_{\gamma\gamma})$  is a two-component model constructed from the  $m_{\gamma\gamma}$  distributions of signal and background events,

$$M(m_{\gamma\gamma}) = N_{sig}M_{sig}(m_{\gamma\gamma}) + N_{bkg}M_{bkg}(m_{\gamma\gamma}), \quad (3)$$

where  $M_{sig}(m_{\gamma\gamma}), M_{bkg}(m_{\gamma\gamma})$  are the shapes of the signal and background  $m_{\gamma\gamma}$  distributions from the simulation, respectively. The expected numbers of signal and background events  $N_{sig}, N_{bkg}$  in the range 0-500 MeV/ $c^2$  are the parameters determined from the fit. After the fit, a background rate of  $541 \pm 37$  events is obtained by integrating the curve  $N_{bkg}M_{bkg}(m_{\gamma\gamma})$  over the mass peak region from 75 MeV/ $c^2$  to 195 MeV/ $c^2$ , the same range as

required by the event selection. The fit reduces the background normalization by a factor of 0.8 compared to the simulation prediction.

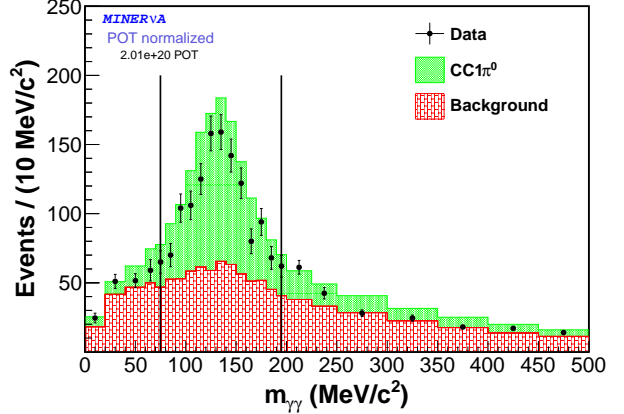


Figure 1: Distribution of the invariant mass of the  $\gamma\gamma$  pair. Data are shown as solid circles with statistical error bars. The shaded histograms show the Monte Carlo predictions for  $CC1\pi^0$  signal (top) and for background (bottom). The signal is defined as antineutrino charged-current events with single  $\pi^0$  and no  $\pi^\pm$  escaping the nucleus. The background is anything else that is not signal. The vertical lines indicate the invariant mass cut,  $75 \text{ MeV}/c^2 < m_{\gamma\gamma} < 195 \text{ MeV}/c^2$ .

The estimated background is subtracted from the total distribution. This background-subtracted data distribution is unfolded to account for detector resolution effects using a Bayesian unfolding method [46] with two iterations. The migration matrix used in the unfolding is obtained from the simulation. The reconstruction efficiency and acceptance corrections are made by dividing by an efficiency curve derived from the simulation. Dividing this corrected distribution by the integrated flux ( $2.5 \times 10^{-8} \bar{\nu}_\mu/\text{cm}^2/\text{POT}$ ) of antineutrinos with energies in the range 1.5-20 GeV, and the number of nucleons in the fiducial volume ( $3.30 \times 10^{30}$ ) gives the differential cross section.

The total uncertainties on the measured cross sections are 20-25% with comparable contributions from statistical and systematic uncertainties. The largest systematic uncertainty is due to the integrated flux uncertainty at 10%. A detailed discussion of the flux systematic uncertainty is presented in Ref. [6]. The next largest contribution to the systematic uncertainty is the 8% normalization uncertainty from the background fit. The other smaller contributions include the neutrino cross-section models, FSI models, and detector simulation systematics. These systematic uncertainties enter the measured cross sections through background subtraction, detector resolution, and efficiency corrections. The neutrino cross-section model and FSI model uncertainties are evaluated by GENIE. The systematic uncertainties on the estimated background is small since the background rate is constrained by data. Systematic errors in the detector response must be inde-

pendently estimated. The uncertainty in neutron response is evaluated by changing the neutron inelastic cross section within experimental uncertainties [47–54] through event reweighting. The reweighting is applied to the leading neutron in the event. A large fraction of the secondary  $\pi^0$  in the background is estimated to arise from  $\pi^- \rightarrow \pi^0$  CEX, for which the cross sections are poorly known. The effect of this uncertainty on our measurement is evaluated by changing the CEX cross section within its uncertainty of  $\pm 50\%$  [43, 55, 56], and then re-measuring the cross sections. Finally, the electromagnetic energy scale uncertainty (2.2%) is taken from the fitted mean uncertainty of the data  $m_{\gamma\gamma}$  distribution. Flux-integrated single differential cross sections in  $\pi^0$  momentum and angle with statistical, systematic, and total uncertainties are summarized in Tables.<sup>5</sup>

#### 4. Results and discussion

The measured differential cross sections as function of  $\pi^0$  momentum and angle with respect to the beam direction are shown in Figures. 2 and 3, respectively. The data are compared to the predictions from GENIE with and without FSI. Above 0.7 GeV/c, FSI effects have little influence on the  $\pi^0$  momentum distribution, and both predictions are in good agreement with the data. For momenta below 0.3 GeV/c, inclusion of FSI gives an increased and shifted cross section relative to the no FSI case. This trend is exhibited by the data; GENIE calculations with and without FSI give a  $\chi^2$  of 25.4 and 50.0 for 11 degrees of freedom (dof), respectively. For the distribution of  $\pi^0$  production angle in Fig. 3, inclusion of FSI into the GENIE simulation results in a mild flattening of the distribution with no significant improvement in the  $\chi^2$  compared to the no FSI case, 16.7 versus 16.0 for 11 degrees of freedom. Thus the effects of FSI are more pronounced with respect to  $\pi^0$  momenta than with  $\pi^0$  production angle. This situation likely reflects the influence of the  $\Delta(1232)$  resonance, which gives a particularly strong momentum dependence to the pion-nucleus interaction for  $p_\pi \approx 0.26$  GeV/c where the pion-carbon cross section is maximum.

Figures. 2 and 3 also show predictions including FSI from the NuWro and NEUT event generators. Any prediction requires knowledge of  $\bar{\nu}_\mu N \rightarrow \mu^+ \pi^0 N$  reactions. Because of the dearth of data for these channels, the calculations use isospin relations to extrapolate from other pion production channels [22, 57]. Both NuWro and NEUT use full cascade models [58] for the FSI description. The  $\chi^2/\text{dof}$  values for the NuWro and NEUT comparisons are 25.0/11 and 24.9/11 for the  $\pi^0$  momentum and 11.8/11 and 14.0/11 for the  $\pi^0$  production angle, respectively. These  $\chi^2$  values indicate that a common level of agreement is achieved by all three generators for  $\pi^0$  momentum, and

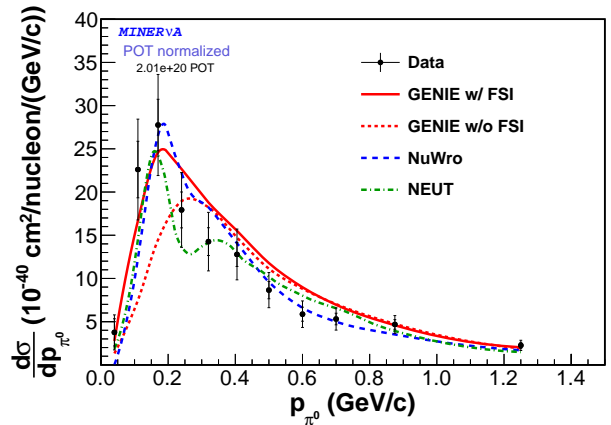


Figure 2: Differential cross section for  $1\pi^0$  production as function of  $\pi^0$  momentum. Data are shown as solid circles. The inner (outer) error bars correspond to statistical (total) uncertainties. The solid (dashed) histograms are GENIE prediction with (without) FSI, the long-dashed histogram is the prediction from the NuWro generator, and the dot-dashed histogram is the prediction from NEUT.

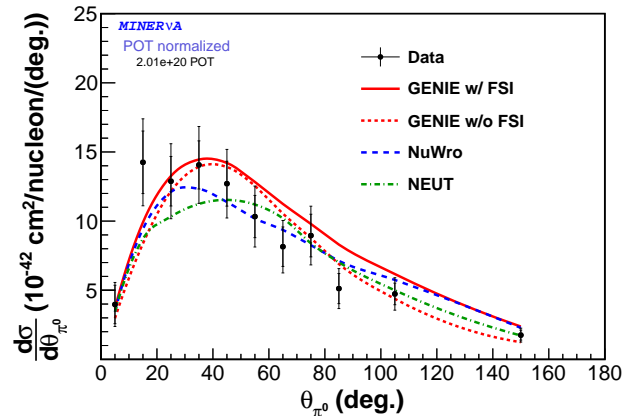


Figure 3: Differential cross section for  $1\pi^0$  production as function of the  $\pi^0$  polar angle. Data are shown as solid circles. The inner (outer) error bars correspond to statistical (total) uncertainties. The solid (dashed) histograms are GENIE prediction with (without) FSI, the long-dashed histogram is the prediction from the NuWro generator, and the dot-dashed histogram is the prediction from NEUT.

that modest differences with predictions versus data are observed for  $\pi^0$  production angle.

There are uncertainties in the FSI used in all calculations. Each assumes the pion FSI after production in the nuclear medium is the same as for pion beams; this assumes no medium effects beyond Fermi momentum and a simple binding energy. Since  $\pi^0$  beams are not possible, isospin relations must be used for  $\pi^0$  FSI. Experiments like these are valuable for testing these approximations. In spite of these uncertainties, the calculations give adequate descriptions of these new data.

<sup>5</sup>See Supplemental Material in the Appendix

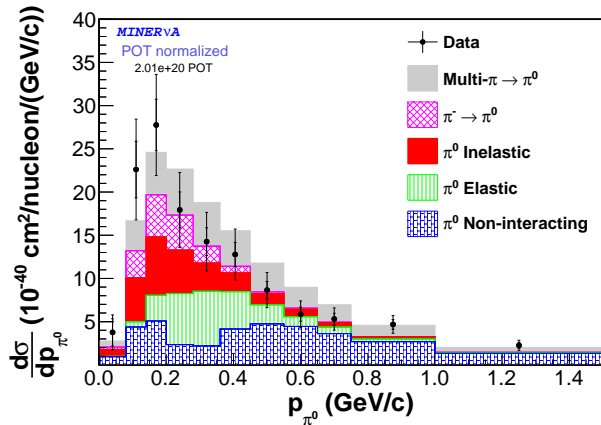


Figure 4: Same cross section data as Fig. 2. The stacked histograms show a decomposition of the  $1\pi^0$  signal into different FSI channels as predicted by GENIE. Description of the FSI channels follows (from top to bottom): 1) Multi- $\pi \rightarrow \pi^0$ : multi-pion produced by the primary interaction and all other pions are re-absorbed inside the nucleus, except a  $\pi^0$ , 2)  $\pi^- \rightarrow \pi^0$ : a  $\pi^-$  produced by the primary interaction, then charge exchanges inside the nucleus, 3)  $\pi^0$  produced by the primary interaction and then undergoing inelastic scattering inside the nucleus, 4)  $\pi^0$  produced by the primary interaction and then undergoing elastic scattering inside the nucleus, and 5)  $\pi^0$  produced by the primary interaction and exiting the nucleus without interacting.

Figures. 4 and 5 show decompositions of the  $\pi^0$  momentum and angle spectra of Figures. 2 and 3 according to the FSI channels as predicted by the GENIE simulation, allowing for a more detailed interpretation. This shows how each FSI process changes the spectrum and gives an indication of what refinements are needed for better agreement with data. GENIE predicts that about 80% of the events undergo some FSI. In the momentum spectrum, absorption events (not shown in the spectrum because the pion disappears in the nucleus) preferentially deplete the region centered at  $p_\pi \approx 0.26$  GeV/c, the momentum where the pion-carbon total reaction cross section is a maximum [42]. On the other hand, pion inelastic scattering and CEX interactions shift the pion momentum from high values to lower values, therefore contributing to the buildup of events at  $p_\pi \approx 0.2$  GeV/c seen in the data. The contributions from multi-pion production followed by absorption, elastic scattering, and the non-interacting component have no noticeable effect on shape.

For the angle spectrum FSI decomposition (Fig. 5) the effects are very different. The interactions displayed in the figure have a small influence on shape and the angular distribution of the  $\Delta(1232)$  decay becomes important. The inelastic and CEX interactions are largely responsible for the buildup of events at backward angles.

Comparison of the observed spectral shape in Fig. 4 to the GENIE prediction suggests that an increase in inelastic scattering together with compensating reduction in elastic and/or multiple-pion production with absorption, could

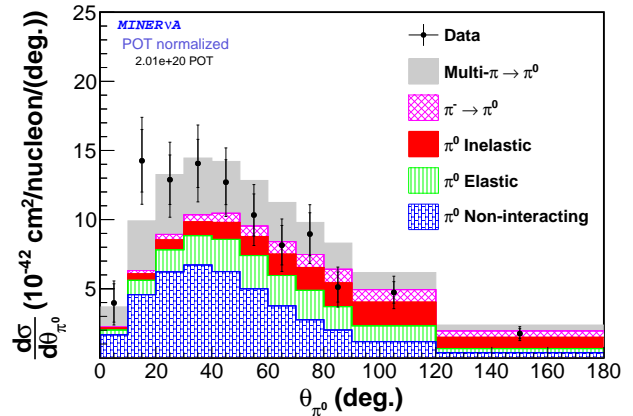


Figure 5: Same cross section data as Fig. 3 and same decomposition as with Fig. 4. The stacked histograms show a decomposition of the  $1\pi^0$  signal into different FSI channels as predicted by GENIE.

improve the agreement with data. On the other hand, Fig. 5 indicates such changes would worsen the agreement with the data for pion production at backwards angles. Thus it appears that a refined description might require separate, independent adjustments to the two spectra.

While the previously reported information on the reaction studied here is too limited to enable comparisons, it is useful to compare with the recently reported MINERVA observations on  $\nu_\mu$  induced charged pion production [20]. The latter data was obtained using a low-energy exposure in the same beamline, and the cross section normalizations are carried out in a similar way for both analyses. Existence of both results provides stronger constraints on the calculations. The  $\pi^0$  momentum range in this analysis is wider than the range shown for the charged pions of Ref. [20] (0-1.5 GeV/c versus 0.1-0.5 GeV/c) because the  $\pi^+$  data is limited by tracking and particle identification requirements. Nevertheless, both analyses show that GENIE predictions are significantly improved when FSI are accounted for. Both results show a peak in the momentum distribution at  $p_\pi \approx 0.2$  GeV/c which is seen in the GENIE calculations, but do not have the correct distribution at energies near this peak. The GENIE predictions for the absolute rates for singly-produced pions exceed the observed rates in both analyses, however the discrepancy is less severe for production by  $\bar{\nu}_\mu$  as reported here.

## 5. Conclusion

The single differential cross sections in  $\pi^0$  momentum and angle have been measured for  $1\pi^0$  production by  $\bar{\nu}_\mu$  charged-current interactions in plastic scintillator (CH). The measurements are found to be in agreement with the predictions from GENIE, NuWro, and NEUT event generators. This agreement is interesting because of the approximations needed to make predictions for this channel. The

measured cross section in  $\pi^0$  momentum disfavors the GENIE prediction without FSI effects at low  $\pi^0$  momentum, which is not surprising since FSI is expected for hadrons inside nuclei. A decomposition of the FSI effects shows that inelastic scattering and CEX reactions are responsible for the peak at  $p_\pi \approx 0.2$  GeV/c. These contributions could be adjusted within external experimental errors to achieve even better agreement of calculations with the  $\pi^0$  momentum data. However, these changes would not be as effective for the  $\pi^0$  polar angle.

Charged-current single pion production in the few GeV region of neutrino energy is an important class of interactions in long-baseline neutrino oscillation experiments. This work presents the first detailed measurements of the kinematic distributions for single  $\pi^0$ s produced in charged current  $\bar{\nu}_\mu$  interactions on carbon. These distributions provide constraints on antineutrino-induced  $\pi^0$  backgrounds as will occur in  $\bar{\nu}_e$  appearance experiments.

## Acknowledgments

This work was supported by the Fermi National Accelerator Laboratory under US Department of Energy contract No. DE-AC02-07CH11359 which included the MINERvA construction project. Construction support also was granted by the United States National Science Foundation under Award PHY-0619727 and by the University of Rochester. Support for participating scientists was provided by NSF and DOE (USA) by CAPES and CNPq (Brazil), by CoNaCyT (Mexico), by CONICYT (Chile), by CONCYTEC, DGI-PUCP and IDI/IGI-UNI (Peru), by Latin American Center for Physics (CLAF) and by RAS and the Russian Ministry of Education and Science (Russia). We thank the MINOS Collaboration for use of its near detector data. Finally, we thank the staff of Fermilab for support of the beamline and the detector.

## References

## References

- [1] L. Alvarez-Ruso, Y. Hayato, J. Nieves, Progress and open questions in the physics of neutrino cross sections at intermediate energies, *New J. Phys.* 16 (2014) 075015. [arXiv:1403.2673](#), [doi:10.1088/1367-2630/16/7/075015](#).
- [2] D. S. Ayres, et al., NOvA Proposal to Build a 30 Kiloton Off-Axis Detector to Study Neutrino Oscillations in the Fermilab NuMI Beamline, [arXiv:hep-ex/0503053](#).
- [3] T. Akiri, et al., The 2010 Interim Report of the Long-Baseline Neutrino Experiment Collaboration Physics Working Groups, [arXiv:1110.6249](#).
- [4] A. A. Aguilar-Arevalo, et al., Measurement of muon neutrino quasi-elastic scattering on carbon, *Phys. Rev. Lett.* 100 (2008) 032301. [arXiv:0706.0926](#), [doi:10.1103/PhysRevLett.100.032301](#).
- [5] V. Lyubushkin, et al., A Study of quasi-elastic muon neutrino and antineutrino scattering in the NOMAD experiment, *Eur.Phys.J. C*63 (2009) 355–381. [arXiv:0812.4543](#), [doi:10.1140/epjc/s10052-009-1113-0](#).

- [6] L. Fields, J. Chvojka, et al., Measurement of Muon Antineutrino Quasi-Elastic Scattering on a Hydrocarbon Target at  $E_\nu \sim 3.5$  GeV, *Phys. Rev. Lett.* 111 (2013) 022501. [arXiv:1305.2234](#).
- [7] A. A. Aguilar-Arevalo, et al., Measurement of neutrino-induced charged-current charged pion production cross sections on mineral oil at  $E_\nu \sim 1$  GeV, *Phys. Rev. D* 83 (2011) 052007. [doi:10.1103/PhysRevD.83.052007](#).
- [8] O. Lalakulich and U. Mosel, Pion production in the Mini-BooNE experiment, *Phys. Rev. C* 87 (2013) 014602. [doi:10.1103/PhysRevC.87.014602](#).
- [9] E. Hernández, J. Nieves, and M.J. Vicente Vacas, Single  $\pi$  production in neutrino nucleus scattering, *Phys. Rev. D* 87 (2013) 113009. [doi:10.1103/PhysRevD.87.113009](#).
- [10] P. Rodrigues, Comparing pion production models to Mini-BooNE data [arXiv:1402.4709](#).
- [11] J. Y. Yu, E. Paschos, I. Schienbein, Comparison of the ANP model with the data for neutrino induced single pion production from the MiniBooNE and MINERvA experiments, *Phys.Rev. D*91 (5) (2015) 054038. [arXiv:1411.6637](#), [doi:10.1103/PhysRevD.91.054038](#).
- [12] H. J. Grabosch, et al., *Z. Phys. C* 41 (1989) 527.
- [13] D. Allasia, et al., *Nucl. Phys. B* 343 (1990) 285.
- [14] S. Barish, et al., *Phys. Rev. D* 19 (1979) 2521.
- [15] G. Radecky, et al., *Phys. Rev. D* 25 (1982) 1161.
- [16] T. Kitagaki, et al., *Phys. Rev. D* 34 (1986) 2554.
- [17] A. A. Aguilar-Arevalo, et al., The MiniBooNE Detector, *Nucl. Instrum. Meth. A* 599 (2009) 28–46. [arXiv:0806.4201](#), [doi:10.1016/j.nima.2008.10.028](#).
- [18] C. Mariani, Neutral pion cross section measurement at K2K, *AIP Conf.Proc.* 967 (2007) 174–178. [doi:10.1063/1.2834471](#).
- [19] Y. Kurimoto, et al., Measurement of Inclusive Neutral Current Neutral  $\pi^0$  Production on Carbon in a Few-GeV Neutrino Beam, *Phys.Rev. D*81 (2010) 033004. [arXiv:0910.5768](#), [doi:10.1103/PhysRevD.81.033004](#).
- [20] B. Eberly, et al., Charged Pion Production in  $\nu_\mu$  Interactions on Hydrocarbon at  $\langle E_\nu \rangle = 4.0$  GeV [arXiv:1406.6415](#).
- [21] A. Aguilar-Arevalo, et al., *Phys. Rev. D* 83 (2011) 052009.
- [22] D. Rein, L. M. Sehgal, Neutrino Excitation of Baryon Resonances and Single Pion Production, *Annals Phys.* 133 (1981) 79–153. [doi:10.1016/0003-4916\(81\)90242-6](#).
- [23] K. Abe, et al., The T2K Experiment, *Nucl. Instrum. Meth. A* 659 (2011) 106–135. [arXiv:1106.1238](#), [doi:10.1016/j.nima.2011.06.067](#).
- [24] A. A. Aguilar-Arevalo, et al., Event Excess in the Mini-BooNE Search for  $\bar{\nu}_\mu \rightarrow \bar{\nu}_e$  Oscillations, *Phys. Rev. Lett.* 105 (2010) 181801. [arXiv:1007.1150](#), [doi:10.1103/PhysRevLett.105.181801](#).
- [25] C. Andreopoulos, et al., The GENIE neutrino Monte Carlo generator, *Nucl. Instrum. Meth. A* 614 (1) (2010) 87–104, Program version 2.6.2 used here. [doi:10.1016/j.nima.2009.12.009](#).
- [26] C. Juszczak, J. A. Nowak, J. T. Sobczyk, Simulations from a new neutrino event generator, *Nucl. Phys. Proc. Suppl.* 159 (2006) 211–216. [arXiv:hep-ph/0512365](#), [doi:10.1016/j.nuclphysbps.2006.08.069](#).
- [27] T. Golan, J. Sobczyk, J. Zmuda, NuWro: the Wroclaw Monte Carlo Generator of Neutrino Interactions, *Nucl. Phys. Proc. Suppl.* 229-232 (2012) 499. [doi:10.1016/j.nuclphysbps.2012.09.136](#).
- [28] Y. Hayato, A neutrino interaction simulation program library NEUT, *Acta Phys.Polon. B*40 (2009) 2477–2489.
- [29] K. Anderson, et al., The NuMI Facility Technical Design Report, *Fermilab-design-1998-01* (1998).
- [30] S. Agostinelli, et al., Geant4 simulation toolkit, *Nucl. Instrum. Meth. A* 506 (3) (2003) 250–303. [doi:10.1016/S0168-9002\(03\)01368-8](#).
- [31] J. Allison, et al., Geant4 developments and applications, *Nuclear Science, IEEE Transactions on* 53 (1) (2006) 270–278. [doi:10.1109/TNS.2006.869826](#).
- [32] C. Alt, et al., Inclusive production of charged pions in p+C collisions at 158-GeV/c beam momentum, *Eur. Phys. J. C*49 (2007) 897–917. [arXiv:hep-ex/0606028](#), [doi:10.1140/epjc/](#)



- s10052-006-0165-7.
- [33] D. Barton, G. Brandenburg, W. Busza, T. Dobrowolski, J. Friedman, et al., Experimental Study of the  $a$ -Dependence of Inclusive Hadron Fragmentation, *Phys.Rev. D* 27 (1983) 2580. doi:10.1103/PhysRevD.27.2580.
- [34] A. V. Lebedev, Ratio of pion kaon production in proton carbon interactions, FERMILAB-THESIS-2007-76.
- [35] L. Aliaga, et al., Design, Calibration, and Performance of the MINERvA Detector, *Nucl. Instrum. Meth. A* 743 (2013) 130. arXiv:1305.5199.
- [36] D. G. Michael, et al., The Magnetized steel and scintillator calorimeters of the MINOS experiment, *Nucl. Instrum. Meth. A* 596 (2008) 190–228. arXiv:0805.3170, doi:10.1016/j.nima.2008.08.003.
- [37] L. Aliaga, et al., MINERvA neutrino detector response measured with test beam data, *Nucl.Instrum.Meth. A* 789 (2015) 28–42. arXiv:1501.06431, doi:10.1016/j.nima.2015.04.003.
- [38] J. Beringer, et al., Review of Particle Physics (RPP), *Phys. Rev. D* 86 (2012) 010001. doi:10.1103/PhysRevD.86.010001.
- [39] A. Bodek, I. Park, U.-K. Yang, Improved low  $Q^2$  model for neutrino and electron nucleon cross sections in few GeV region, *Nucl. Phys. Proc. Suppl.* 139 (2005) 113–118. arXiv:hep-ph/0411202, doi:10.1016/j.nuclphysbps.2004.11.208.
- [40] G. Radecky, et al., Study of Single Pion Production by Weak Charged Currents in Low-energy Neutrino  $d$  Interactions, *Phys. Rev. D* 25 (1982) 1161–1173.
- [41] T. Kitagaki, et al., Study of  $\nu d \rightarrow \mu^- pp_s$  and  $\nu d \rightarrow \mu^- \Delta^{++}(1232)n_s$  using the BNL 7-foot deuterium filled bubble chamber, *Phys. Rev. D* 42 (1990) 1331–1338. doi:10.1103/PhysRevD.42.1331.
- [42] T. Lee, R. Redwine, Pion nucleus interactions, *Ann. Rev. Nucl. Part. Sci.* 52 (2002) 23–63.
- [43] D. Ashery, et al., True Absorption and Scattering of Pions on Nuclei, *Phys. Rev. C* 23 (1981) 2173–2185.
- [44] C. Anderson, et al., The ArgoNeuT detector in the NuMI low-energy beam line at Fermilab, *Journal of Instrumentation* 7 (2012) 10019.
- [45] R. J. Barlow, C. Beeston, Fitting using finite Monte Carlo samples, *Comput.Phys.Commun.* 77 (1993) 219–228, as implemented in TFractionFitter, ROOT framework. doi:10.1016/0010-4655(93)90005-W.
- [46] G. D’Agostini, A multidimensional unfolding method based on Bayes’ theorem, *Nucl. Instrum. Meth. A* 362 (1995) 487–498. doi:10.1016/0168-9002(95)00274-X.
- [47] W. P. Abfalterer, et al., Measurement of neutron total cross-sections up to 560-MeV, *Phys. Rev. C* 63 (2001) 044608. doi:10.1103/PhysRevC.63.044608.
- [48] W. Schimmerling, et al., Neutron-nucleus total and inelastic cross-sections - 900 to 2600 MeV/c, *Phys. Rev. C* 7 (1973) 248–262. doi:10.1103/PhysRevC.7.248.
- [49] R. G. P. Voss, R. Wilson, *Proc. Roy. Soc.* A236 (1956) 41.
- [50] I. Slypen, V. Corcalciuc, J. P. Meulders, Proton and deuteron production in neutron-induced reactions on carbon at  $E(n) = 42.5, 62.7,$  and  $72.8$  MeV, *Phys. Rev. C* 51 (1995) 1303–1311. doi:10.1103/PhysRevC.51.1303.
- [51] J. Franz, et al., Neutron induced production of protons, deuterons and tritons on copper and bismuth, *Nucl. Phys. A* 510 (1990) 774–802. doi:10.1016/0375-9474(90)90360-X.
- [52] U. Tippawan, et al., Light-ion production in the interaction of 96-MeV neutrons with carbon, *Phys. Rev. C* 79 (2009) 064611. arXiv:0812.0701, doi:10.1103/PhysRevC.79.064611.
- [53] R. Bevilacqua, et al., Light-ion production from O, Si, Fe and Bi induced by 175 MeV quasi-monoenergetic neutrons arXiv:1303.4637.
- [54] C. I. Zanelli, et al., Total non-elastic cross sections of neutrons on C, O, Ca, and Fe at 40.3 and 50.4 MeV, *Phys. Rev. C* 23 (1981) 1015–1022. doi:10.1103/PhysRevC.23.1015.
- [55] T. Bowles, D. Geesaman, R. Holt, H. Jackson, J. Julien, et al., Inclusive ( $\pi^\pm, \pi^0$ ) Reactions in Nuclei, *Phys.Rev. C* 23 (1981) 439–447. doi:10.1103/PhysRevC.23.439.
- [56] M. Jones, R. Ransome, V. Cupps, R. Ferguson, C. Morris, et al., Pion absorption above the Delta (1232) resonance, *Phys.Rev. C* 48 (1993) 2800–2817. doi:10.1103/PhysRevC.48.2800.
- [57] K. Graczyk, D. Kielczewska, P. Przewlocki, J. Sobczyk,  $C_5^A$  axial form factor from bubble chamber experiments, *Phys. Rev. D* 80 (2009) 093001. arXiv:0908.2175, doi:10.1103/PhysRevD.80.093001.
- [58] L. Salcedo, E. Oset, M. Vicente-Vacas, C. Garcia-Recio, Computer simulation of inclusive pion nuclear reactions, *Nucl. Phys. A* 484 (1988) 557. doi:10.1016/0375-9474(88)90310-7.



## 6. Appendix

This Appendix contains additional tables that are referenced in the article.

Table 1: Flux-averaged differential cross section in  $\pi^0$  momentum,  $d\sigma/dp_{\pi^0}$  ( $10^{-40}\text{cm}^2/\text{nucleon}/(\text{GeV}/c)$ ), for  $1\pi^0$  production with statistical (stat), systematic (sys), and total (tot) uncertainties.

$p_{\pi^0}$ (GeV/c)	$d\sigma/dp_{\pi^0}$	stat(%)	sys(%)	tot(%)
0.00 - 0.08	3.75	41	33	53
0.08 - 0.14	22.60	14	21	25
0.14 - 0.20	27.75	10	18	21
0.20 - 0.28	17.92	11	21	24
0.28 - 0.36	14.26	11	20	23
0.36 - 0.45	12.77	10	20	22
0.45 - 0.55	8.65	11	20	23
0.55 - 0.65	5.86	13	22	26
0.65 - 0.75	4.67	12	20	24
0.75 - 1.00	2.25	11	18	21
1.00 - 1.50	1.27	15	21	26

Table 2: Flux-averaged differential cross section in  $\pi^0$  angle,  $d\sigma/d\theta_{\pi^0}$  ( $10^{-42}\text{cm}^2/\text{nucleon}/\text{deg.}$ ), for  $1\pi^0$  production with statistical (stat), systematic (sys), and total (tot) uncertainties.

$\theta_{\pi^0}$ (deg.)	$d\sigma/d\theta_{\pi^0}$	stat(%)	sys(%)	tot(%)
0 - 10	3.97	34	19	40
10 - 20	14.25	15	15	22
20 - 30	12.88	13	15	21
30 - 40	14.06	12	15	19
40 - 50	12.70	12	15	19
50 - 60	10.32	14	15	21
60 - 70	8.14	17	15	23
70 - 80	8.95	17	16	23
80 - 90	5.11	21	18	28
90 - 120	4.73	16	18	24
120- 180	1.75	20	20	28

## SUPPLEMENTAL MATERIAL

This supplemental material contains additional tables that are referenced in the article.

TABLE I: Flux-averaged differential cross section in  $\pi^0$  momentum,  $d\sigma/dp_{\pi^0}$  ( $10^{-40}$  cm<sup>2</sup>/nucleon/(GeV/c), for  $1\pi^0$  production with statistical (stat), systematic (sys), and total (tot) uncertainties.

$p_{\pi^0}$ (GeV/c)	$d\sigma/dp_{\pi^0}$	stat(%)	sys(%)	tot(%)
0.00 - 0.08	3.75	41	33	53
0.08 - 0.14	22.60	14	21	25
0.14 - 0.20	27.75	10	18	21
0.20 - 0.28	17.92	11	21	24
0.28 - 0.36	14.26	11	20	23
0.36 - 0.45	12.77	10	20	22
0.45 - 0.55	8.65	11	20	23
0.55 - 0.65	5.86	13	22	26
0.65 - 0.75	4.67	12	20	24
0.75 - 1.00	2.25	11	18	21
1.00 - 1.50	1.27	15	21	26

TABLE II: Flux-averaged differential cross section in  $\pi^0$  angle,  $d\sigma/d\theta_{\pi^0}$  ( $10^{-42}$  cm<sup>2</sup>/nucleon/deg.), for  $1\pi^0$  production with statistical (stat), systematic (sys), and total (tot) uncertainties.

$\theta_{\pi^0}$ (deg.)	$d\sigma/d\theta_{\pi^0}$	stat(%)	sys(%)	tot(%)
0 - 10	3.97	34	19	40
10 - 20	14.25	15	15	22
20 - 30	12.88	13	15	21
30 - 40	14.06	12	15	19
40 - 50	12.70	12	15	19
50 - 60	10.32	14	15	21
60 - 70	8.14	17	15	23
70 - 80	8.95	17	16	23
80 - 90	5.11	21	18	28
90 - 120	4.73	16	18	24
120- 180	1.75	20	20	28